Advanced Composites and Hybrid Materials (2022) 5:1477–1489
https://doi.org/10.1007/s42114-022-00509-z

ORIGINAL RESEARCH

Enhanced energy storage of lead-free mixed oxide core double-shell barium strontium zirconate titanate@magnesium aluminate@zinc oxide-boron trioxide-silica ceramic nanocomposites

Rong Ma[1] · **Bin Cui**[2] · **Dengwei Hu**[1] · **Salah M. El-Bahy**[3] · **Yan Wang**[1] · **Islam H. El Azab**[4] · **Ashraf Y. Elnaggar**[4] · **Hongxi Gu**[1] · **Gaber A. M. Mersal**[5] · **Mina Huang**[6,7] · **Vignesh Murugadoss**[6]

Received: 12 March 2022 / Revised: 5 May 2022 / Accepted: 24 May 2022 /

Abstract

$Ba_{0.8}Sr_{0.2}Zr_{0.1}Ti_{0.9}O_3$@MgO-$Al_2O_3$@ZnO-$B_2O_3$-$SiO_2$ (BSZT@MgO-Al_2O_3@ZBSO) core double-shell lead-free nanoceramic is prepared by facile protocol. The protocol involves three steps of (a) BSZT synthesis by co-precipitation, (b) coating of MgO-Al_2O_3 layer through co-precipitation, and (c) ZBSO deposition via sol-precipitation method. The diameter of the resultant BSZT@MgO-Al_2O_3@ZBSO core double-shell nanoparticles is about 280 nm, and the average thicknesses of the MgO-Al_2O_3 and ZBSO layers are about 8 and 13 nm, respectively. The physical and chemical properties of BSZT@MgO-Al_2O_3@ZBSO are tuned by varying the ratio between MgO and Al_2O_3 of MgO-Al_2O_3 layer. The results reveal that the grain size increases with the decrease in the MgO/Al_2O_3 ratio, while the dielectric properties initially increase and then decrease with increase of Al_2O_3 content. After sintering at 1150 °C for 2 h, the MgO-Al_2O_3 in the interlayer self-assembled into a $MgAl_2O_4$ spinel phase. Thus, fine-grained relaxor ferroelectric BSZT@$MgAl_2O_4$@ZBSO core double-shell ceramic nanoceramics (grain size $\leq$ 300 nm) were obtained. The lead-free core double-shell nanoparticles with Mg/Al ratio of 4:2 exhibit the maximum energy storage density of 0.91 J/cm^3 under a maximum polarization field of 28.08 kV/mm.

Keywords Core double-shell nanoparticles · Self-assembly · Fine-grained ceramics · Relaxor ferroelectric · Energy storage

1 Introduction

With the increasing awareness of environmental pollution [1–5], people have made great efforts to pursue sustainable materials [6–8] and green energy types including batteries, phase change energy, solar, and capacitors [9–16]. Dielectric energy storage capacitors have been playing indispensable roles in modern electronic and electrical devices, including electric armors, electric guns, particle beam accelerators, high-power microwave sources, ballistic missile systems, and hybrid electrical vehicles [17–19]. Among the dielectric materials that can be used in energy storage devices,

---

✉ Rong Ma
marong20@126.com

✉ Bin Cui
cuibin@nwu.edu.cn

[1] Faculty of Chemistry and Chemical Engineering, Key Laboratory of Phytochemistry of Shaanxi Province, Engineering Research Center of Advanced Ferroelectric Functional Materials, BaojiUniversity of Arts and Sciences, 1 Hi-Tech Avenue, Baoji 721013, Shaanxi, China

[2] Key Laboratory of Synthetic and Natural Functional Molecule Chemistry of Ministry of Education, Shaanxi Key Laboratory of Physico-Inorganic Chemistry, College of Chemistry and Materials Science, Northwest University, Xi’an 710127, Shaanxi, China

[3] Department of Chemistry, Turabah University College, Taif University, Taif 21944, Saudi Arabia

[4] Department of Food Science and Nutrition, College of Science, Taif University, Taif 21944, Saudi Arabia

[5] Department of Chemistry, College of Science, Taif University, Taif 21944, Saudi Arabia

[6] Advanced Materials Division, Engineered Multifunctional Composites Nanotech, LLC, Knoxville, TN 37934, USA

[7] College of Materials Science and Engineering, Taiyuan University of Science and Technology, Taiyuan 030024, China

dielectric ceramics have attracted much attention because of their high power density, fast charge/discharge rate, and excellent thermal stability [20, 21]. However, the relatively low energy storage density has become a major disadvantage limiting the application of dielectric ceramics. In addition, the use of lead-containing ceramics is strictly controlled for environmental reasons. Hence, there is an urgent need to develop lead-free dielectric ceramics with higher energy storage properties to further improve the overall performance of power electronic devices.

Generally, the energy storage density (W), recoverable energy storage density (Wrec), and energy storage efficiency (η) of dielectric ceramics are calculated by integration of areas between the charging and discharging curves of displacement-electric field loops (D-E) and polarization axis, which can be described by Eqs. (1)–(3), respectively [22].

$$W = \int_0^{P_{max}} EdD \tag{1}$$

$$W_{rec} = \int_{P_r}^{P_{max}} EdD \tag{2}$$

$$\eta = \frac{W_{rec}}{W} \tag{3}$$

where P_r is the remnant polarization, Pmax is the maximum polarization, and E is the applied electric field. It can be indicated from the above equations that high dielectric breakdown strengths (BDS), high Pmax, and low Pr are all essential to simultaneously achieve high Wrec and high η. Among many candidates for dielectric ceramics, including linear dielectrics, antiferroelectrics, and ferroelectrics [23, 24], relaxor ferroelectrics have been considered as the most potential candidate because of their high maximum polarization ($P_{\max}$) and low remnant polarization (P_r) [25, 26]. Moreover, their polarization can be maintained to temperatures higher than Curie temperature due to the existence of polar nanoregions (PNRs).

The $Ba_{1-x}Sr_xTi_{1-y}Zr_yO_3$ are promising relaxor ferroelectric ceramics for energy storage due to their good dielectric and electrical properties over a wide range of temperatures and frequencies and environmentally friendly composition [27]. Applications with high energy density have led to increasing concern over the dielectric breakdown strength (BDS) which is critical in determining the energy storage capacity [28]. Therefore, numerous investigations of the ceramics that are suitable for energy storage have focused on their high BDS, and have found that this property is influenced by several factors, such as secondary phase (such as MgO, Al_2O_3, or ZnO [29, 30]), porosity, grain size, structure, and defects [31, 32]. Huang et al. [33] reported the production of a BST-MgO composite ceramic using spark plasma sintering (SPS), which speeded up the sintering rate enough to let MgO exist at the grain boundaries, thereby improving BDS. Especially, when MgO and Al_2O_3 are coated together, spinel $MgAl_2O_4$ with higher BDS will be formed during the sintering process, which will be beneficial to increase the BDS of the ceramics [34]. However, the presence of MgO and Al_2O_3 decreases the sintering performance, and SPS is too expensive for use in high-volume production and difficult to scale up [35]. Alternatively, the addition of a range of glasses has been shown to improve BDS while improving sintering performance and refining the microstructure, leading to a transition from a diffusion phase to relaxor behavior [36, 37]. Young et al. [38] added BaO-SiO_2-Al_2O_3-B_2O_3-ZrO_2-SrO glass to $BaTiO_3$, and found that the BDS increased to 2.8 times that of pure $BaTiO_3$ at 20 vol% of the glass. Zhang et al. [39] found that BST ceramics containing 20 vol% of BaO-SiO_2-B_2O_3 glass had the highest average BDS (23.9 kV/mm), which is 1.9 times that of pure BST, and the ceramics had a grain size < 1 μm. To meet the growing demand for high energy density and miniaturization, there is an increasing need to develop fine-grained ceramics that can be used in multi-layer structures with very thin layers [40, 41]. The development of particles with a core–shell structure has been emphasized for the fabrication of multi-layer ceramic capacitors, especially for ceramics with good temperature stability, because this structure can inhibit the growth of grains [42]. At the same time, researchers have begun to study the suitability of particles with a core–shell structure for use in energy storage applications [43]. For example, our research group prepared fine-grained BSZT@MgO@ZBSO ceramics with a multi-level core–shell structure that exhibited the maximum energy storage density of 0.71 J/cm^3 [44]. Therefore, selecting appropriate core and shell materials and designing a microstructure that can improve the BDS and reduce the sintering temperature without degrading the host material properties would be significant advances.

To explore the possibilities, BSZT@MgO-Al_2O_3@ZBSO fine-grained particles were synthesized with the core double-shell structure that are capable of meeting the need for energy storage. The submicron BSZT particles were selected as the core owing to its dielectric relaxation properties. An intermediate layer comprised of MgO and Al_2O_3 was introduced to improve the BDS and decrease the dielectric loss. The glass-phase ZBSO was coated as the outermost coating layer to prepare the dense ceramics under a relatively low sintering temperature. Further, the ratio between MgO and Al_2O_3 of MgO-Al_2O_3 layer is varied to optimize the microstructural and dielectric properties. Moreover, the outermost "shell" ZBSO promoted the self-assembly of MgO and Al_2O_3 in the intermediate layer to form $MgAl_2O_4$ spinel phase upon densification at 1150 °C for 2 h. The microstructural, dielectric, and energy storage characteristics were investigated using X-ray diffraction, electron microscopy, impedance, and ferroelectric analyzer methods. Compared with MgO as the intermediate layer, $MgAl_2O_4$ effectively improved the BDS of the material, thereby improved the energy storage properties. The lead-free core double-shell nanoparticles with Mg/Al ratio of 4:2 exhibit the maximum energy storage density of 0.91 J/cm^3 under a maximum 8 kV/mm.

2 Experimental

2.1 Synthesis

The precursors, $Ba(CH_3COO)_2$, $Sr(CH_3COO)_2 \cdot 0.5H_2O$, $Zr(NO_3)_4 \cdot 5H_2O$, $TiCl_4$, $Mg(CH_3COO)_2$, $Al(NO_3)_3$, $Zn(NO_3)_2 \cdot 6H_2O$, tetraethoxysilane (TEOS), $C_{12}H_{27}BO_3$ (tributyl borate), and NaOH, are obtained from the Shanghai Chemical Reagent Factory (Shanghai, China). All the chemicals are of analytical-grade chemicals (with a minimum purity of 99%). The BSZT@MgO-Al_2O_3@ZBSO particles and ceramics were prepared with 2.0 mol% MgO and 0.5, 1.0, 1.5, and 2.0 mol% Al_2O_3 with Mg/Al ratios of 4:1, 4:2, 4:3, and 4:4, respectively. The content of ZBSO was 4.0 wt%.

Synthesis of the BSZT@MgO-Al_2O_3 particles The submicron BSZT particles were prepared via co-precipitation with the stoichiometric composition of $Ba_{0.8}Sr_{0.2}Zr_{0.1}Ti_{0.9}O_3$ following the reported procedure [45]. Then prepared BSZT particles were suspended in deionized water (1 g/300 mL) by means of ultrasonic dispersion for 30 min. Then, 7.0 mL of 0.013 mol/L $Mg(CH_3COO)_2$ (2.0 mol% MgO) solution was slowly added to the slurries. Then, according to the stoichiometric ratio (Al_2O_3 content of 0.5, 1.0, 1.5, 2.0 mol%, respectively), four parts of $Al(NO_3)_3$ solution were separately added to the above four suspensions. The pH of these suspension were maintained at the values greater than 9 by adding ammonia. After additional reaction for 1 h, BSZT@MgO-Al_2O_3 core–shell structured particles were obtained by drying the total slurry and calcined the residues at 750 °C for 2 h in an air atmosphere.

Synthesis of the BSZT@MgO-Al_2O_3@ZBSO particles and ceramics ZBSO was coated on the surface of BSZT@MgO-Al_2O_3 core–shell structured particles through the sol-precipitation method described in our previous work [46]. The molar ratio of ZnO, B_2O_3, and SiO_2 in the ZBSO was 3.1:1.0:2.8. After the completion of reaction, the solution was centrifuged to collect the resultant precipitate was dried at 150 °C for 3 h to obtain BSZT@MgO-Al_2O_3@ZBSO core double-shell nanoceramics. Of the polyvinyl alcohol (PVA), 7 wt.% is added to the BSZT@MgO-Al_2O_3@ZBSO core double-shell nanoceramics as binder to make disk-shaped pellets at 6-MPa pressure. These pellets were sintered in air at 1150 °C for 2 h to produce the test samples. To measure the dielectric properties, silver paste was painted on the polished samples as the electrodes and the samples were annealed at 830 °C for 15 min. Figure 1 illustrates the design and preparation of fine-grained BSZT@$MgAl_2O_4$@ZBSO energy storage ceramics.

2.2 Characterization

The crystal microstructures were identified using X-ray diffractometer (XRD; D8 Advance, Bruker, Frankfurt, Germany) with Cu-Kα radiation (Kα = 1.54059 Å). The morphology of the particles was characterized using field-emission transmission electron microscopy (FE-TEM; Tecnai G2 F20S-TWIN, FEI, Hillsboro, OR, USA) with energy-dispersive spectroscopic (EDS) analysis. The morphology of the ceramic samples was characterized using a field-emission scanning electron microscope (FE-SEM; Model JSM-5800, JEOL, Tokyo, Japan). The *P-E* hysteresis loops were measured using a ferroelectric tester (Model 609B, Radiant technology, Washington, USA). Dielectric properties were measured using an LCR meter (Model HP4284A, Hewlett-Packard Company, CA, USA) controlled by a computer. The capacitances of the ceramics were determined by a HP 4284A LCR at 1 V_{rms} from − 60 to 150 °C, increasing at rate of 2 °C/min.

3 Results and discussion

3.1 Phase composition and morphology of the BSZT@MgO-Al_2O_3@ZBSO powders

Figure 2 shows the crystalline structure of BSZT@MgO-Al_2O_3@ZBSO core double-shell nanoceramics with different MgO and Al_2O_3 ratios. All the samples are coated with the same content (4.0 wt%) of ZBSO. All samples exhibit the tetragonal phase perovskite structure with a diffraction split corresponding to (002)/(200) planes at 45°–46°. The magnified image shows that the peak corresponding to the (002)/(200) facet broadens as the ratio between MgO and Al_2O_3 is reduced. The more detailed discussion on the effect of MgO and Al_2O_3 ratio on phase composition is discussed later in Sect. 3.2. No impurity (secondary phase) peak is detected in the X-ray diffraction pattern of BSZT@MgO-Al_2O_3@ZBSO core double-shell nanoceramics. This is because that MgO and Al_2O_3 form a barrier layer on the surface of the BSZT particles, which prevents the diffusion of Mg^{2+} and Al^{3+} ions into the lattice [47].

Figure 3 shows the TEM image and EDS line scan analysis of BSZT@MgO-Al_2O_3@ZBSO core double-shell nanoceramics with MgO/Al_2O_3 ratio of 4:2. It depicts that the BSZT@MgO-Al_2O_3@ZBSO have uniform spherical

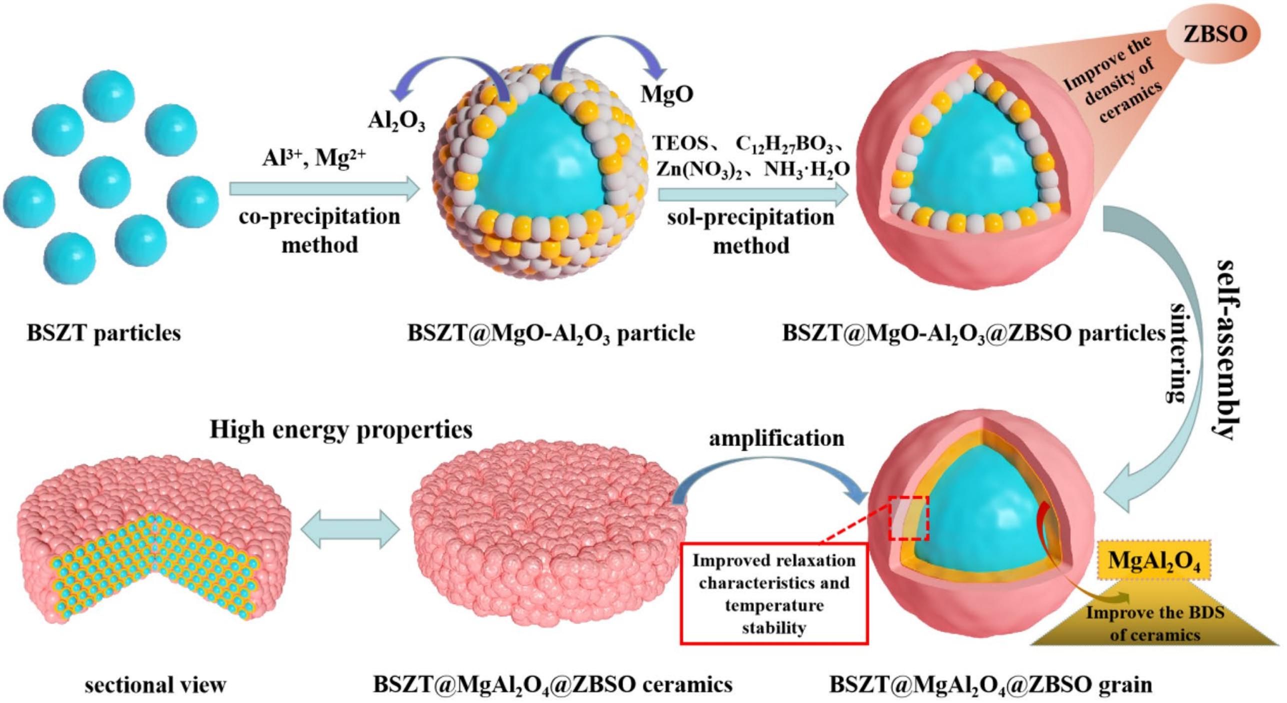

Fig. 1 The illustration of the design and the preparation of fine-grained BSZT@$MgAl_2O_4$@ZBSO energy storage ceramics

morphology with an average diameter of about 280 nm. Figure 3b shows a single BSZT@MgO-Al_2O_3@ZBSO core double-shell nanoparticle. The interior (core) and edge (shell) of the spherical particles show distinctly different contrasts, indicating that the shell layer material is successfully coated on the BSZT surface. According to the EDS line scan analysis along the straight line AB, Zn, B, and Si are distributed in the outermost layer of the core double-shell nanoparticles, indicating that the outermost layer of the particles is ZBSO. The average thickness of ZBSO shell is about 13 nm. Two sharp peaks of Mg and Al appear next to the inner side of the ZBSO layer, indicating that MgO and Al_2O_3 form an intermediate shell coating next to of ZBSO. The average thickness of MgO-Al_2O_3 layer is about 8 nm. The above results confirm that the BSZT forms the "core," the MgO-Al_2O_3 forms the intermediate shell, and the ZBSO forms the outermost shell for of the BSZT@MgO-Al_2O_3@ZBSO core double-shell nanoceramics. The mechanism for the formation of coating layers, MgO, Al_2O_3, and ZBSO, on the surface of monodisperse BSZT nanoparticles by precipitation method involves two direct steps First, $Mg(Ac)_2$ and $Al(NO_3)_3$ solutions were heterogeneously nucleated in

Fig. 2 XRD patterns for BSZT@MgO-Al_2O_3@ZBSO core double-shell nanoceramics with different MgO/Al_2O_3 ratios in MgO-Al_2O_3 layer: (**a**) 4:1, (**b**) 4:2, (**c**) 4:3, and (**d**) 4:4

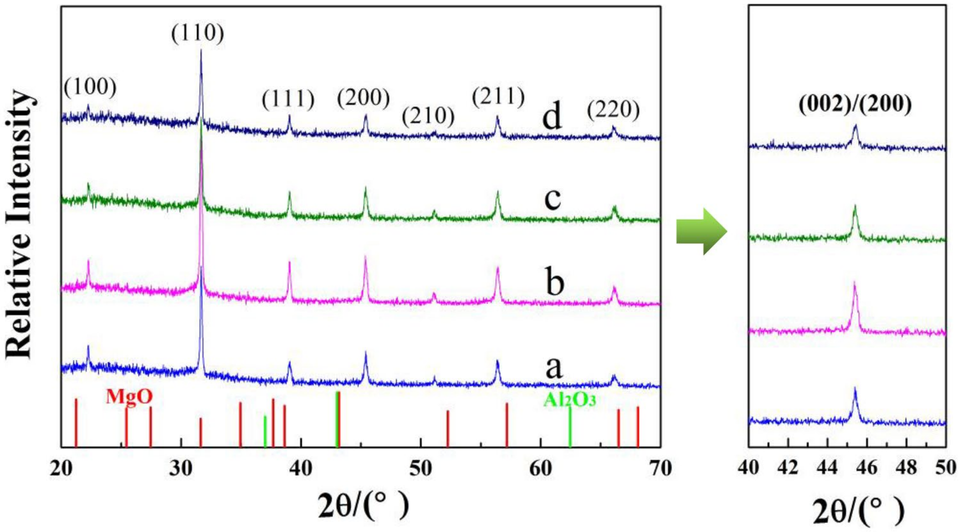

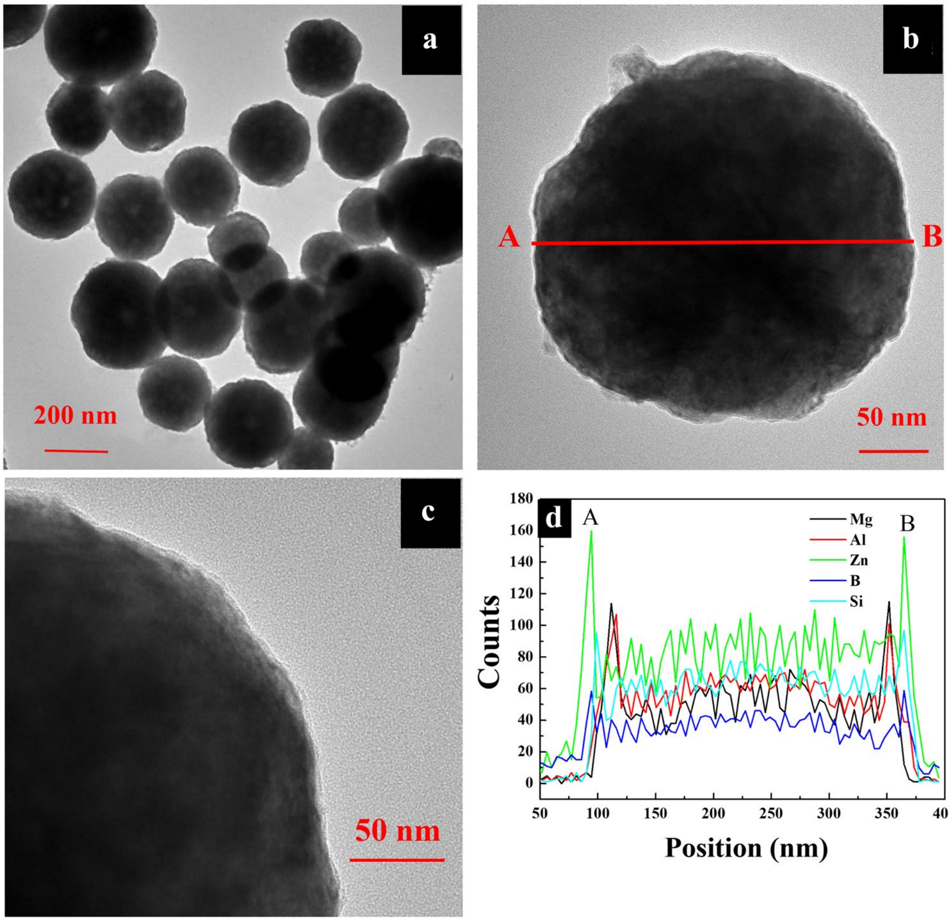

Fig. 3 (**a**)–(**c**)TEM image of BSZT@MgO-Al_2O_3@ZBSO core double-shell nanoceramics with MgO/Al_2O_3 ratio of 4:2 and (**d**) EDS results of line-scan microanalysis of the BSZT@MgO-Al_2O_3@ZBSO core double-shell nanoceramics along the line from A to B

BSZT suspensions at pH ~ 9 to form $Mg(OH)_2$ and $Al(OH)_3$ on the surface of BSZT particles, which were then calcined to form BSZT@MgO-Al_2O_3. Secondly, ZBSO is coated on the surface of BSZT@MgO-Al_2O_3 particle to form the outermost shell layer.

3.2 Effect of the MgO/Al_2O_3 ratio on the phase composition and morphology of the BSZT@MgO-Al_2O_3@ZBSO ceramics

Figure 4 shows the XRD patterns of the BSZT@MgO-Al_2O_3@ZBSO ceramics with different MgO/Al_2O_3 ratios. All the nanoceramic samples exhibit tetragonal phase perovskite structure. With increasing Al_2O_3 content, the $MgAl_2O_4$ spinel phase is detected from the ratio of 4:2 to the ratio of 4:4; characteristic peak of $MgAl_2O_4$ (~ 27.5°) becomes prominent. This is because the outermost shell ZBSO promotes the reaction between MgO and Al_2O_3, which leads to the self-assembly of $MgAl_2O_4$ spinel phase to form the BSZT@$MgAl_2O_4$@ZBSO core double-shell nanoceramics [48]. The magnified image of (002)/(200) diffraction peak depicts a slight move towards higher angle with decrease in the MgO/Al_2O_3 ratio from 4:1 to 4:3. On further decreasing the MgO/Al_2O_3 ratio to 4:4, the (002)/(200) diffraction peak moves slightly toward the lower angle. This may be related to the substitution of ions in the BSZT lattice. At a lower ratio, due to a smaller radius than Mg^{2+}, a small amount of Al^{3+} enters the BSZT lattice first (promoted by ZBSO), causing the shift to a higher angle. However, at a higher ratio, the Al^{3+} content is high and therefore Al_2O_3 is shared with the outermost layer ZBSO, promoting the entry of Mg^{2+} into the BSZT lattice causing the shift towards lower angle. The general formula for the perovskite structure is ABO_3, where the A ion occupies the apex position of the face-centered cube, and the B ion occupies the face center position. The tolerance factor (t) for stable perovskite structure can be calculated from the following formula [49]:

$$t = \frac{r_A + r_o}{\sqrt{2}(r_B + r_o)} \tag{4}$$

where r_A represents the ionic radius of the atoms at A site, r_B represents the ionic radius of the atoms at B site, and r_O represents the oxygen ion radius. The t value in the range between 0.77 and 1.10 leads to a stable perovskite structure. The closer the t value is to 1, the more stable the perovskite

Fig. 4 XRD patterns for BSZT@MgO-Al_2O_3@ZBSO core double-shell nanoceramics with different MgO/Al_2O_3 ratios in MgO-Al_2O_3 layer: (**a**) 4:1, (**b**) 4:2, (**c**) 4:3, and (**d**) 4:4

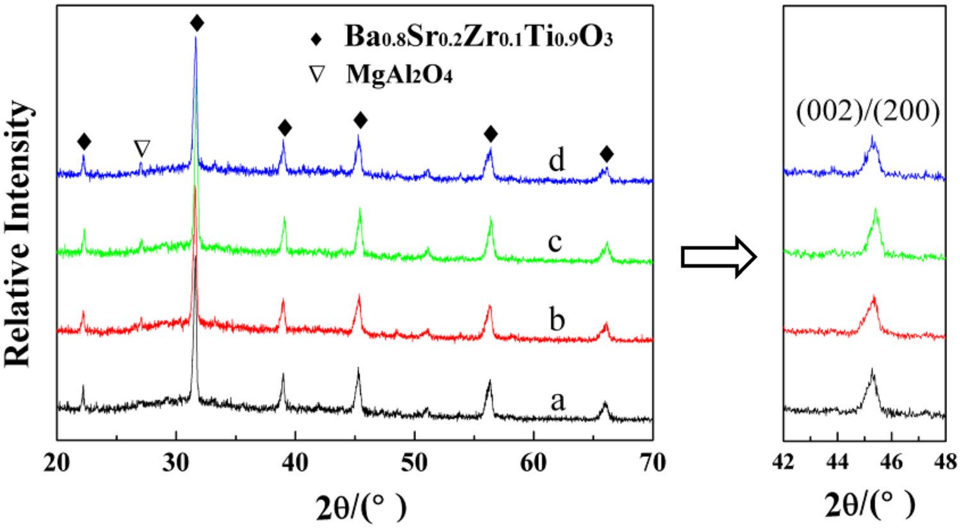

structure is. For a t value of less than 0.77, the ilmenite structure is formed, and for a t value of more than 1.10, the calcite structure is formed. In the $Ba_{0.8}Sr_{0.2}Zr_{0.1}Ti_{0.9}O_3$ system, r_A is the weighted average of the ionic radius of Ba^{2+} (0.135 nm) and Sr^{2+} (0.113 nm), and r_B is the weighted average of the ionic radius of Ti^{4+} (0.064 nm) and $Zr.^{4+}$ (0.087 nm). The average value is calculated as

$$r_A = 0.8 \cdot r\left(Ba^{2+}\right) + 0.2 \cdot r(Sr^{2+}) \quad (5)$$

$$r_B = 0.1 \cdot r\left(Zr^{4+}\right) + 0.9 \cdot r(Ti^{4+}) \quad (6)$$

For the pure $Ba_{0.8}Sr_{0.2}Zr_{0.1}Ti_{0.9}O_3$ system, the calculated r_A is 0.1306 nm and the r_B is 0.0663 nm. The tolerance factors for the entry of Mg^{2+} and Al^{3+} into the lattice are listed in Table 1. Although Mg^{2+} has the same valence as Ba^{2+} and Sr^{2+}, t is closer to 1 when occupying the B site, indicating that Mg^{2+} is more likely to enter the BSZT as lattice replacement for Ti^{4+}. Similarly, the t is closer to 1 when Al^{3+} replaces the B site instead of A site. Therefore, a small amount of Mg^{2+} and Al^{3+} replaces the B site, and the substitution between ions of different valence creates ionic vacancies and charge defects, while the system still retains the original perovskite structure. The lattice distortion is caused as Al^{3+} being substituted at the B site since the radius of Al^{3+} is smaller than r_B, resulting in the decrease in the interplanar spacing such that the (002)/(200) diffraction peak moves towards higher angle. The interplanar spacing is increased when Mg^{2+} is substituted at the B position since the radius of Mg^{2+} is larger than r_B, which in turn causes the (002)/(200) diffraction peak to move towards lower angle [50].

Table 1 The tolerance factor of the dopant of Mg^{2+} and Al^{3+}

Doped ions	Ion radius (nm)	Replace position	t
Mg^{2+}	0.072	A	0.7268
		B	0.9026
Al^{3+}	0.050	A	0.6514
		B	1.0070

Figure 5 shows the FE-SEM images and grain-size distribution (inset) of the BSZT@$MgAl_2O_4$@ZBSO core double-shell nanoceramics with different MgO/Al_2O_3 ratio and the EDS analysis spectrum of the ceramics with a MgO/Al_2O_3 ratio of 4:3. As the MgO/Al_2O_3 ratio decreases, the densification of the ceramic increases, and the size of ceramic grains increases slightly (average grain sizes of a, b, c, d are 254 nm, 272 nm, 289 nm, 301 nm, respectively). This is because the Al_2O_3 remaining in the shell or at the grain boundary inhibit the growth of ceramic grains. In addition, MgO and Al_2O_3 composite coating can promote the sintering of ceramics [37, 51]. Therefore, when the amount of Al_2O_3 is relatively large, it still promote sintering together with the outermost layer (ZBSO), and the liquid phase will fully infiltrate the solid particles during the sintering process to accelerate the ion mass transfer process, which is beneficial to the formation of fine-grained dense ceramics. The ceramic grains are compactly arranged, exhibiting excellent densification. Especially when MgO/Al_2O_3 = 4:3, the grain size of ceramics is more uniform and has a compact microscopic morphology. This is due to the lower melting point of MgO-Al_2O_3 composite, and the formation of liquid phase by outermost shell layer ZBSO to promote ceramic sintering to densify [52, 53]. Figure 5e, f show the FE-SEM and EDS analysis of ceramics at MgO/Al_2O_3 = 4:3, respectively. The distribution of Zn, B, and Si at the grain boundaries is higher than that inside the grains. Significant peaks appear in the 0–13 nm of shell layer and in the 276–289 nm of the spherical nanoceramics, indicating that Zn, B, and Si are

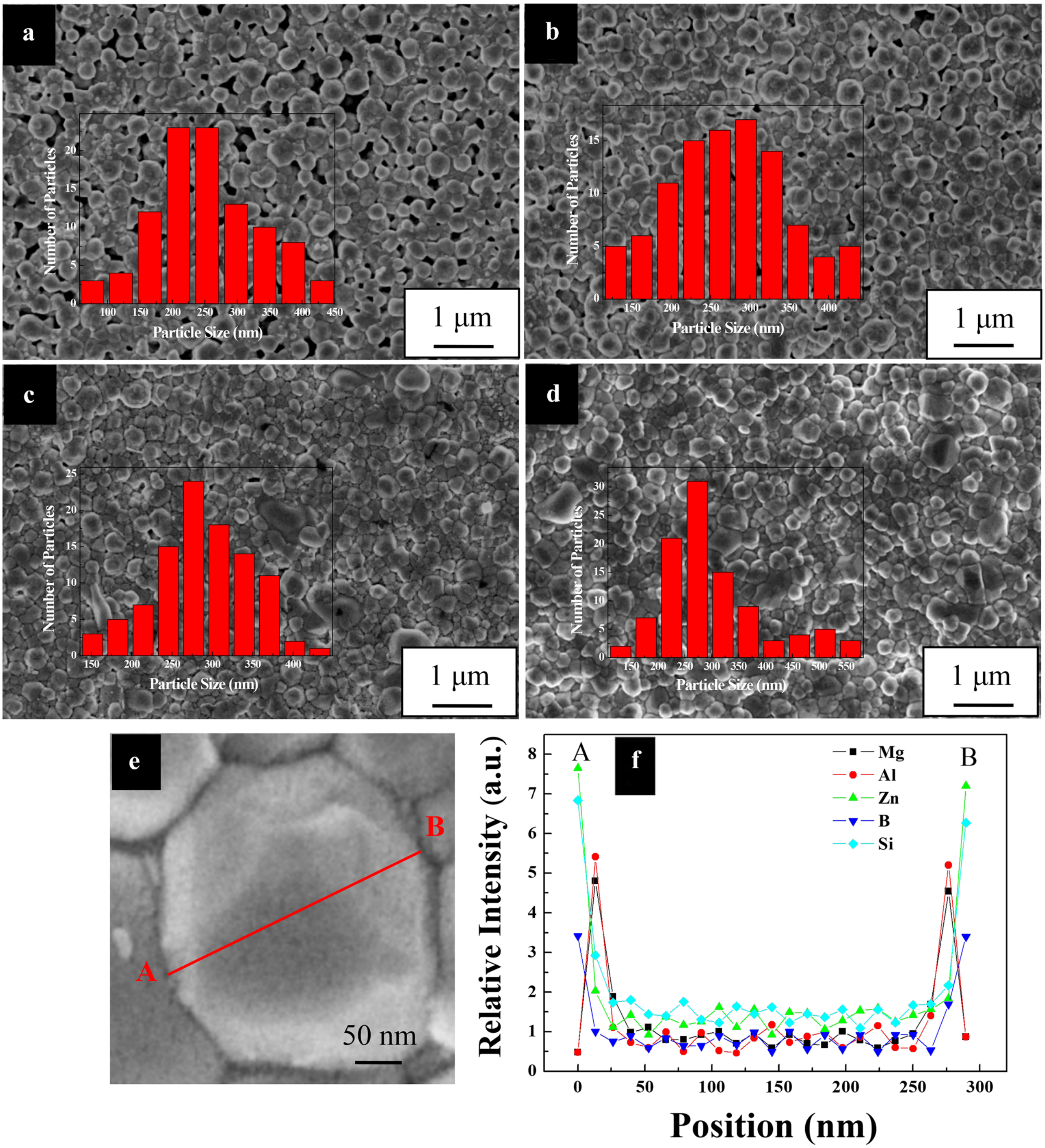

Fig. 5 FE-SEM images and grain-size distribution (inset) for BSZT@$MgAl_2O_4$@ZBSO core double-shell nanoceramics with different MgO/Al_2O_3 ratios: (**a**) 4:1, (**b**) 4:2, (**c**) 4:3, and (**d**) 4:4. (**e**) FE-SEM image for the BSZT@MgO-Al_2O_3@ZBSO grain. (**f**) EDS results of line-scan microanalysis of the BSZT@MgO-Al_2O_3@ZBSO grain along the line from A to B in Fig. 5e

mainly distributed in the outer layer of the grain. Two sharp peaks corresponding to Mg and Al appear in the vicinity of Zn, B, and Si, indicating that Mg and Al exist in the middle layer of BSZT@$MgAl_2O_4$@ZBSO core double-shell nanoceramic grains. Therefore, the grain size of BSZT@$MgAl_2O_4$@ZBSO ceramics basically maintains the structure of the particles with a double-layer "core–shell" structure, indicating that the fine-grained ceramics with controlled microstructure are prepared by the method of double-layer coating and further sintering.

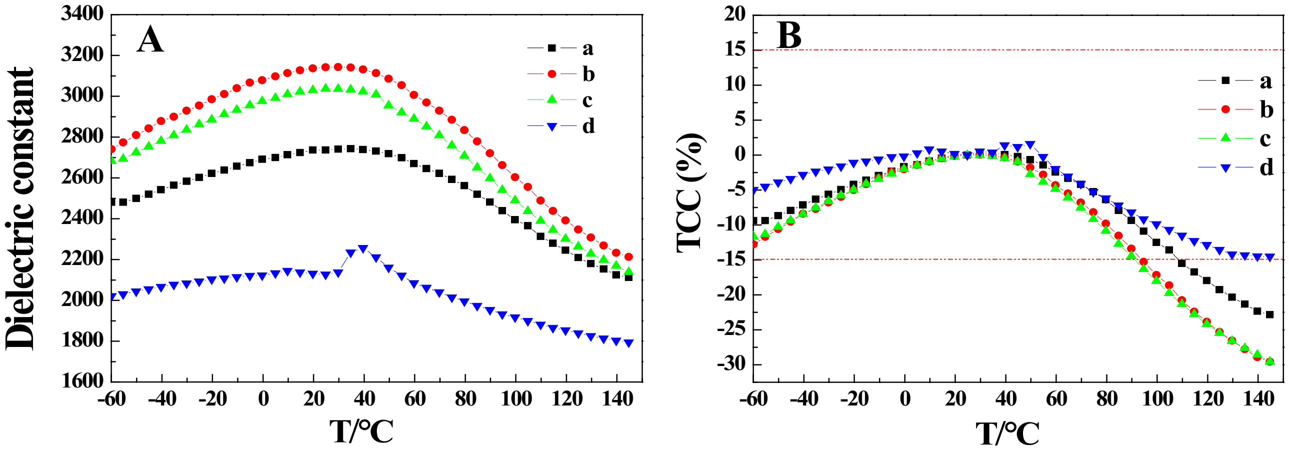

Fig. 6 Temperature dependence of (A) the dielectric constant (ε_r) and (B) the temperature capacitance characteristic (TCC) for BSZT@$MgAl_2O_4$@ZBSO core double-shell nanoceramics with different MgO/Al_2O_3 ratios (**a**) 4:1, (**b**) 4:2, (**c**) 4:3, and (**d**) 4:4

3.3 Effect of the MgO/Al_2O_3 ratio on the dielectric, BDS, and energy storage properties of the BSZT@$MgAl_2O_4$@ZBSO ceramics

Figure 6 demonstrates the temperature dependence of the dielectric constant and temperature capacitance characteristics (TCC) at 1 kHz over the temperature range from − 60 to 150 °C for all the nanoceramic samples. The dielectric constant initially increases and then decreases with the decrease in the MgO/Al_2O_3 ratio. When the MgO/Al_2O_3 ratio is 4:2, the dielectric constant is the highest, reaching 3143. This is because the uniformity of the particles was promoted by the Al_2O_3 coating, which increased the dielectric constant. However, as the coating amount of Al_2O_3 increases, the dielectric constant reduced due to the intrinsic low dielectric constant of Al_2O_3. The ceramic meets the X8R standard (55 to + 150 °C, magnitude of the temperature–capacitance characteristic (TCC) within ± 15%) when the MgO/Al_2O_3 ratio is 4:4, which may be because the multi-layered core–shell structure is more conducive to the improvement of ceramic temperature stability. There is no obvious change in the Curie temperature (T_c). This may be due to several reasons. First, as the MgO/Al_2O_3 ratio decreases, the ceramic grain size does not change significantly. Second, $MgAl_2O_4$ stays in the middle shell layer and does not diffuse into the lattice, which has little effect on the T_c of the ceramic. Table 2 shows the main parameters of the dielectric properties of ceramics. As the MgO/Al_2O_3 ratio decreases, the dielectric loss of BSZT@MgO-Al_2O_3@ZBSO ceramics at room temperature gradually decreases. This may be because Al^{3+} can absorb jumping electrons between variable ions [54, 55], so as the amount of Al_2O_3 coating increases, the dielectric loss decreases.

Figure 7 shows the dielectric temperature spectrum at different frequencies for BSZT@$MgAl_2O_4$@ZBSO nanoceramics with different MgO/Al_2O_3 ratios. The T_c of all the samples shifts toward the high temperature as the frequency increases, showing good relaxation characteristics [56, 57]. This may be due to the existence of a complex intermediate shell of BSZT@$MgAl_2O_4$@ZBSO ceramics, and its polarization region becomes more complicated in the microscopic region, so the ceramic has good dispersion with typical relaxation behavior [58]. Figure 7e shows the modified Curie–Weiss fit for BSZT@$MgAl_2O_4$@ZBSO nanoceramics with $MgO/Al_2O_3 = 4:2$. When the Mg/Al ratio is 4:2, $r = 1.81$ is calculated from the graph, also indicating that it has good relaxation characteristics. The above research results, combined with the previous XRD, SEM, and dielectric properties, indicate that a fine-grained ceramic material having a core–shell structure similar to the powder can be prepared

Table 2 Main properties of the BSZT@$MgAl_2O_4$@ZBSO ceramics

MgO/Al_2O_3	ε_{max}	Tan δ (25 °C)	ε_r (25 °C)	TCC (%)		
				− 55 °C	T_c	150 °C
4:1	2743	0.0167	2737	− 9.39	0.22	− 22.83
4:2	3143	0.0166	3142	− 11.71	0.03	− 29.57
4:3	3037	0.0142	3037	− 11.33	0	− 29.56
4:4	2161	0.0103	2127	− 4.51	1.60	− 14.50

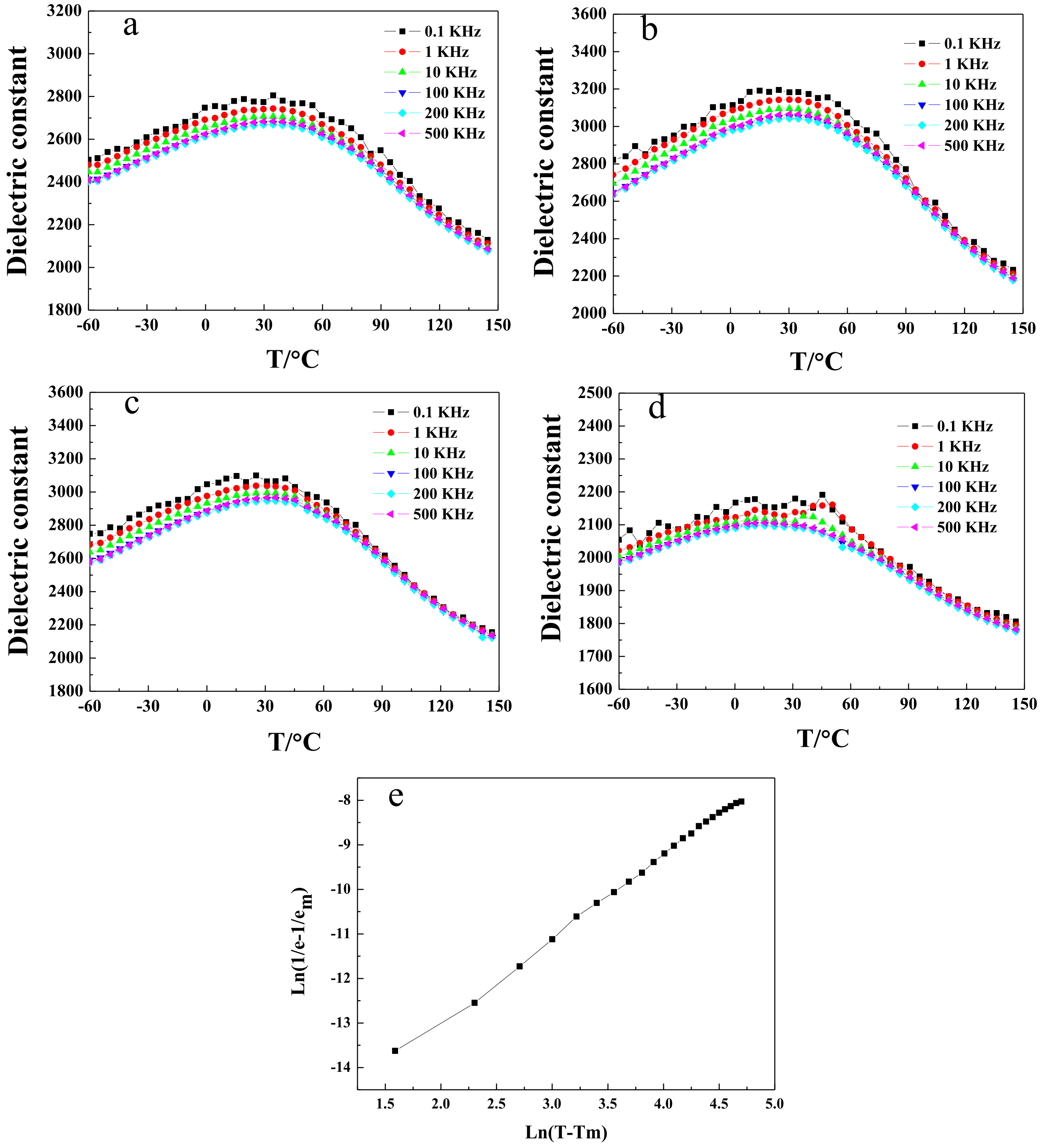

Fig. 7 Temperature dependence of dielectric constant at different measuring frequencies for BSZT@MgAl$_2$O$_4$@ZBSO core double-shell nanoceramics with different MgO/Al$_2$O$_3$ ratios in MgO-Al$_2$O$_3$ layer: (**a**) 4:1, (**b**) 4:2, (**c**) 4:3, and (**d**) 4:4. (**e**) Modified Curie–Weiss fit for BSZT@MgAl$_2$O$_4$@ZBSO nanoceramics with MgO/Al$_2$O$_3$ = 4:2

by effective control of the sintering process. More importantly, through the layered coating of different materials, the dielectric properties and relaxation characteristics can be improved, and the dielectric loss can be reduced, thereby achieving controllable preparation from micronanopowders to fine-grained ceramics, laying the foundation for energy storage applications of miniaturized, high-capacity MLCCs.

Figure 8 shows the Weibull distribution of different MgO/Al$_2$O$_3$ ratios of BSZT@MgAl$_2$O$_4$@ZBSO ceramics. The BDS can be expressed as:

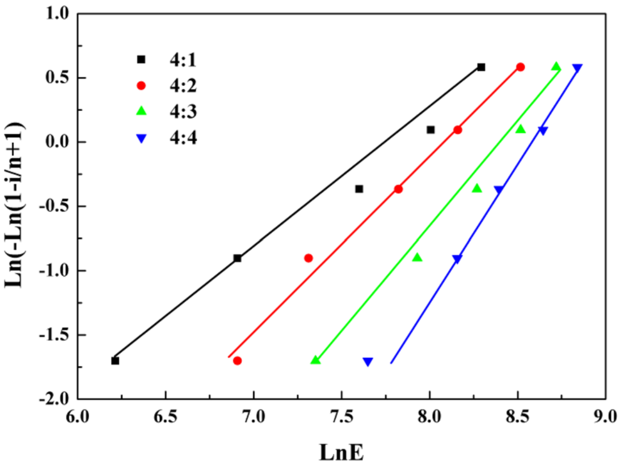

Fig. 8 Weibull distribution for the dielectric breakdown strength of BSZT@$MgAl_2O_4$@ZBSO core double-shell nanoceramics with different MgO/Al_2O_3 ratios in $MgO\text{-}Al_2O_3$ layer (**a**) 4:1, (**b**) 4:2, (**c**) 4:3, and (**d**) 4:4

$$X_i = \ln(E_i) \tag{7}$$

$$Yi = ln[-ln(1 - Pi)] \tag{8}$$

$$Pi = i/(n + 1) \tag{9}$$

where E_i is the electric field strength at each measurement, P_i is the probability of dielectric breakdown, and n is the number of times the sample measured. As the ratio of Al_2O_3 increases, the BDS of the ceramic increases. On the one hand, Al_2O_3 itself has a high BDS, and when it is uniformly coated on the surface of the ceramic grains, the BDS of the ceramic is improved; on the other hand, the formation of the spinel phase $MgAl_2O_4$ increases the BDS of the ceramic significantly. In addition, the coating improves the dispersion and uniformity of the particles, and finally, a fine-grained ceramic material with uniform grains is obtained. The reduction of ceramic grains further plays an important role in the improvement of its BDS [32].

Figure 9 shows the hysteresis loop diagram of different MgO/Al_2O_3 ratios of BSZT@$MgAl_2O_4$@ZBSO ceramics. Table 3 shows the discharged energy density, charged energy density, energy storage efficiency, BDS, and DC resistivity of the ceramics. The hysteresis loops of all the ceramics are narrower. With the decrease of MgO/Al_2O_3 ratio, the linear enhancement of BSZT@$MgAl_2O_4$@ZBSO ceramics, the decrease of the saturation polarization intensity, and the discharge energy storage density of ceramics first increase and then decreases. This may be due to the increase in Al_2O_3 which improves the dispersion of the powder and increases the densification and BDS of the ceramic, thereby increasing the energy storage density. However, when the amount of Al_2O_3 is high, it dilutes the ferroelectric phase and reduces the polarization intensity, which in turn reduces the energy storage density. When the MgO/Al_2O_3 ratio is 4:2, the ceramic has a maximum energy storage density of 0.91 J/cm^3, which is due to the self-assembly of the spinel

Fig. 9 *P-E* hysteresis loops for the BSZT@$MgAl_2O_4$@ZBSO core double-shell nanoceramics with different MgO/Al_2O_3 ratios in $MgO\text{-}Al_2O_3$ layer: (**a**) 4:1, (**b**) 4:2, (**c**) 4:3, and (**d**) 4:4

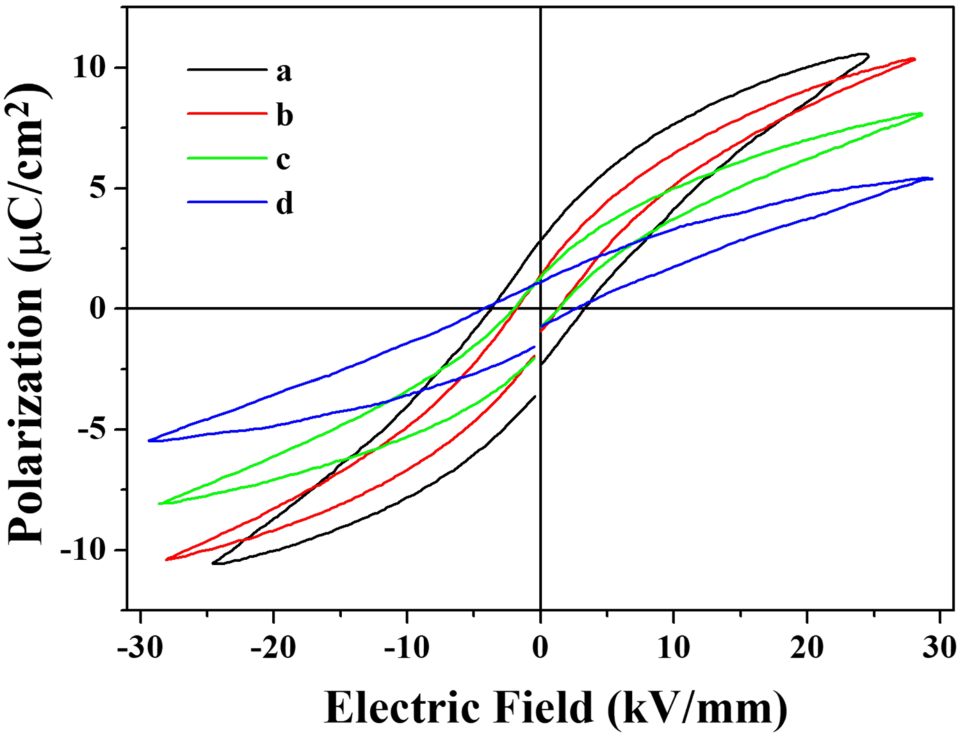

Table 3 The discharged energy density, charged energy density, energy storage efficiency, BDS, and DC resistivity of the samples at room temperature in Fig. 9

Number of samples	*a*	*b*	*c*	*d*
Discharged energy density (J_d, J/cm^3)	0.58	0.70	0.71	0.65
Discharged energy density (J_d; J/cm^3)	0.67	0.91	0.72	0.49
Charged energy density (J_c; J/cm^3)	1.36	1.25	1.01	0.91
Energy storage efficiency (%)	49.3	72.8	71.2	53.8
BDS (kV/mm)	24.59	28.08	28.62	29.40
DC resistivity (× 10^{12} Ω•cm)	2.01	2.45	2.67	2.81

phase $MgAl_2O_4$ that is increasing the BDS of the ceramic. The corresponding DC resistivity is also increased. When the MgO/Al_2O_3 ratio is 4:4, the ceramic resistivity is 2.81×10^{12} Ω•cm, indicating that the insulation performance is improved, which is conducive to the improvement of energy storage density. The energy storage efficiency of ceramics first increases and then decreases. When the MgO/Al_2O_3 ratio is 4:2, the energy storage efficiency of ceramics reaches a maximum of 72.8%. Therefore, the selection of suitable coating materials and the control of the coating amount are particularly important for the improvement of energy storage properties.

4 Conclusion

Using submicron BSZT particles as a starting material, MgO and Al_2O_3 as materials with high BDS, and ZBSO as a sintering agent, we rationally designed core double-shell structural BSZT@MgO-Al_2O_3@ZBSO nanoceramics. MgO-Al_2O_3 in the intermediate layer was self-assembled into $MgAl_2O_4$ spinel phase during sintering at 1150 °C for 2 h, yielding dense, fine-grained relaxation ferroelectric BSZT@$MgAl_2O_4$@ZBSO ceramics (grain size ≤ 300 nm) with excellent energy storage performance. The discharge energy storage of BSZT@$MgAl_2O_4$@ZBSO nanoceramics increases first and then decreases with the decrease in MgO/Al_2O_3 ratio. When the MgO/Al_2O_3 ratio is 4:2, the ceramic has the maximum dielectric constant of 3143 with good dielectric relaxation properties and a maximum energy storage density of 0.91 J/cm^3. When the MgO/Al_2O_3 ratio is 4:3, the ceramic has the maximum BDS of 28.62 kV/mm. The BSZT@$MgAl_2O_4$@ZBSO materials are easy and inexpensive to fabricate, and the improved microstructure and dielectric properties indicate that the core double-shell approach represents a good way to prepare such materials for use in multi-layer energy storage capacitors.

Funding Support was provided by the Shaanxi Provincial Natural Science Basic Research Project (2021JQ-810), Horizontal Project of Shaanxi Province (2021-KJHX001), Horizontal Project of Shaanxi Province (2022-KJHX011), Shaanxi Provincial Department of Education Special Scientific Research Project (grant number 19JK0035), and Taif University Researchers Supporting Project number (TURSP-2020/14), Taif University, Taif, Saudi Arabia.

Declarations

Conflict of interest The authors declare no competing interests.

References

1. Jing C, Zhang Y, Zheng J, Ge S, Lin J, Pan D, Naik N, Guo Z (2022) In-situ constructing visible light CdS/Cd-MOF photocatalyst with enhanced photodegradation of methylene blue. Particuology 69: 111. https://doi.org/10.1016/j.partic.2021.11.013
2. Cheng W, Wang YM, Ge SS, Ding XQ, Cui ZW, Shao Q (2021) One-step microwave hydrothermal preparation of Cd/Zr-bimetallic metal–organic frameworks for enhanced photochemical properties. Adv Compos Hybrid Mater 4:150. https://doi.org/10.1007/s42114-020-00199-5
3. Kumar R, Umar A, Kumar R, Chauhan MS, Kumar G, Han SC (2021) Spindle-like Co_3O_4-ZnO nanocomposites scaffold for hydrazine sensing and photocatalytic degradation of rhodamine B dye. Eng Sci 16:288. https://doi.org/10.30919/es8d548
4. Nandanwar R, Bamne J, Singh N, Taiwade K, Chandel V, Sharma PK, Singh P, Umar A, Haque FZ (2022) Synthesis of titania/silica nanocomposite for enhanced photodegradation of methylene blue and methyl orange dyes under UV and mercury lights. ES Materials and Manufacturing 16:78. https://doi.org/10.30919/esmm5f628
5. Sayyed SA, Beedri NI, Bhujbal PK, Shaikh SF, Pathan HM (2020) Eosin-Y sensitized Bi-layered ZnO nanoflower-CeO2 photoanode for dye-sensitized solar cells application. ES Materials and Manufacturing 10:45. https://doi.org/10.30919/esmm5f939
6. Guo L, Zhang YF, Zheng JJ, Shang LQ, Shi YJ, Wu Q, Liu XX, Wang YM, Shi LQ, Shao Q (2021) Synthesis and characterization of ZnNiCr-layered double hydroxides with high adsorption activities for Cr(VI). Adv Compos Hybrid Mater 4:819. https://doi.org/10.1007/s42114-021-00260-x
7. Zhang FH, Cheng W, Yu ZH, Ge SS, Shao Q, Pan D, Liu B, Wang XJ, Guo ZH (2021) Microwave hydrothermally synthesized WO_3/UiO-66 nanocomposites toward enhanced photocatalytic degradation of rhodamine B. Adv Compos Hybrid Mater 4:1330. https://doi.org/10.1007/s42114-021-00346-6
8. Khater HM, El-Nagar AM (2020) Preparation of sustainable of eco-friendly MWCNT-geopolymer composites with superior sulfate resistance. Adv Compos Hybrid Mater 3:375. https://doi.org/10.1007/s42114-020-00170-4
9. Chen LQ, Zhao YH (2022) From classical thermodynamics to phase-field method. Prog Mater Sci 124:100868. https://doi.org/10.1016/j.pmatsci.2021.100868
10. Zhao YH, Zhang B, Hou H, Chen WP, Wang M (2019) Phase-field simulation for the evolution of solid/liquid interface front in directional solidification process. J Mater Sci Technol 35:1044. https://doi.org/10.1016/j.jmst.2018.12.009
11. Qu KQ, Sun Z, Shi C, Wang WC, Xiao LD, Tian JY, Huang ZH, Guo ZH (2021) Dual-acting cellulose nanocomposites filled with carbon nanotubes and zeolitic imidazolate framework-67 (ZIF-67)–derived polyhedral porous Co_3O_4 for symmetric

supercapacitors. Adv Compos Hybrid Mater 4:670. https://doi.org/10.1007/s42114-021-00293-2

12. Pan D, Su FM, Liu CT, Guo ZH (2020) Research progress for plastic waste management and manufacture of value-added products. Adv Compos Hybrid Mater 3:443. https://doi.org/10.1007/s42114-020-00190-0
13. Ma Y, Xie X, Yang W, Yu Z, Du W (2021) Recent advances in transition metal oxides with different dimensions as electrodes for high-performance supercapacitors. Adv Compos Hybrid Mater 4(4):1–19. https://doi.org/10.1007/s42114-021-00358-2
14. Khan SH, Pathak B, Fulekar MH (2020) A study on the influence of metal (Fe, Bi, and Ag) doping on structural, optical, and antimicrobial activity of ZnO nanostructures. Adv Compos Hybrid Mater 3(1). https://doi.org/10.1007/s42114-020-00174-0
15. Sun J, Mu Q, Kimura H, Murugadoss V, He M, Du W (2022) Oxidative degradation of phenols and substituted phenols in the water and atmosphere: a review. Adv Compos Hybrid Mater 1–14. https://doi.org/10.1007/s42114-022-00435-0
16. Guo J, Chen Z, Abdul W, Kong J, Khan MA, Young DP, Zhu J, Guo Z (2021) Tunable magnetoresistance of core-shell structured polyaniline nanocomposites with 0-, 1-, and 2-dimensional nanocarbons. Adv Compos Hybrid Mater 1–14. https://doi.org/10.1007/s42114-021-00211-6
17. Chu B, Zhou X, Ren K, Neese B, Lin M, Wang Q, Bauer F, Zhang QM (2006) A dielectric polymer with high electric energy density and fast discharge speed. Science 313:334. https://doi.org/10.1126/science.1127798
18. Yao Z, Song Z, Hao H, Yu Z, Cao M, Zhang S, Lanagan MT, Liu H (2017) Homogeneous/inhomogeneous-structured dielectrics and their energy-storage performances. Adv Mater 29:1601727. https://doi.org/10.1002/adma.201601727
19. Sun H, Wang X, Sun Q, Zhang X, Ma Z, Guo M, Sun B, Zhu X, Liu Q, Lou X (2020) Large energy storage density in $BiFeO_3$-$BaTiO_3$-$AgNbO_3$ lead-free relaxor ceramics. J Eur Ceram Soc 40:2929. https://doi.org/10.1016/j.jeurceramsoc.2020.03.012
20. Xu R, Xu Z, Feng Y, He H, Tian J, Huang D (2016) Temperature dependence of energy storage in $Pb_{0.90}La_{0.04}Ba_{0.04}[(Zr_{0.7}$-$Sn_{0.3})_{0.88}Ti_{0.12}]O_3$ antiferroelectric ceramics. J Am Ceram Soc 99:2984. https://doi.org/10.1111/jace.14297
21. Wu S, Li W, Lin M, Burlingame Q, Chen Q, Payzant A, Xiao K, Zhang QM (2013) Aromatic polythiourea dielectrics with ultrahigh breakdown field strength, low dielectric loss, and high electric energy density. Adv Mater 25:1734. https://doi.org/10.1002/adma.201204072
22. Wang H, Cao M, Huang R, Tao C, Pan W, Hao H, Yao Z, Liu H (2021) Preparation of $BaTiO_3$@NiO core-shell nanoparticles with antiferroelectric-like characteristic and high energy storage capability. J Eur Ceram Soc 41:4129. https://doi.org/10.1016/j.jeurceramsoc.2021.02.042
23. Luo B, Wang X, Tian E, Song H, Wang H, Li L (2017) Enhanced energy storage density and high efficiency of lead-free $CaTiO_3$-$BiScO_3$ linear dielectric ceramics. ACS Appl Mater Interfaces 9:19963. https://doi.org/10.1021/acsami.7b04175
24. Xu Y, Guo Y, Liu Q, Wang G, Bai J, Tian J, Lin L, Tian Y (2020) High energy storage properties of lead-free Mn-doped (1-x) $AgNbO_3$-x$Bi_{0.5}Na_{0.5}TiO_3$ antiferroelectric ceramics. J Eur Ceram Soc 40:56. https://doi.org/10.1016/j.jeurceramsoc.2019.09.022
25. Wang T, Jin L, Li C, Hu Q, Wei X (2015) Relaxor ferroelectric $BaTiO_3$–$Bi(Mg_{2/3}Nb_{1/3})O_3$ ceramics for energy storage application. J Am Ceram Soc 98: 559. https://doi.org/10.1111/jace.13325
26. Yuan Q, Yao F, Wang Y, Ma R, Wang H (2017) Relaxor-relaxor-ferroelectric 0.9$BaTiO_3$-0.1$Bi(Zn_{0.5}Zr_{0.5})O_3$ ceramic capacitors with high energy density and temperature stable energy storage properties. J Mater Chem C 5:9552. https://doi.org/10.1039/C7TC02478A
27. Mondal T, Majee BP, Middya TR, Sarun PM (2016) Structural and dielectric relaxation behaviour of $Ba_{0.8}Sr_{0.2}Zr_{0.1}Ti_{0.9}O_3$ ceramic. IOP Conference Series: Mater Sci Eng 149:012168. https://doi.org/10.1088/1757-899x/149/1/012168
28. Wang X, Zhang Y, Song X, Yuan Z, Ma T, Zhang Q, Deng C, Liang T (2012) Glass additive in barium titanate ceramics and its influence on electrical breakdown strength in relation with energy storage properties. J Eur Ceram Soc 32:559. https://doi.org/10.1016/j.jeurceramsoc.2011.09.024
29. Zhang Q, Wang L, Luo J, Tang Q, Du J (2010) $Ba_{0.4}Sr_{0.6}TiO_3$/MgO composites with enhanced energy storage density and low dielectric loss for solid-state pulse-forming line. Int J Appl Ceram Technol 7:E124. https://doi.org/10.1111/j.1744-7402.2009.02456.x
30. Dong G, Ma S, Du J, Cui J (2009) Dielectric properties and energy storage density in ZnO-doped $Ba_{0.3}Sr_{0.7}TiO_3$ ceramics. Ceram Int 35:2069. https://doi.org/10.1016/j.ceramint.2008.11.003
31. Oh J-H, Lee YH, Ju BK, Shin DK, Park C-Y, Oh MH (1997) Impact of surface properties on the dielectric breakdown for polycrystalline and multilayered $BaTiO_3$ thin films. J Appl Phys 82:6203. https://doi.org/10.1063/1.366505
32. Song Z, Liu H, Zhang S, Wang Z, Shi Y, Hao H, Cao M, Yao Z, Yu Z (2014) Effect of grain size on the energy storage properties of $(Ba_{0.4}Sr_{0.6})TiO_3$ paraelectric ceramics. J Eur Ceram Soc 34:1209. https://doi.org/10.1016/j.jeurceramsoc.2013.11.039
33. Huang YH, Wu YJ, Qiu WJ, Li J, Chen XM (2015) Enhanced energy storage density of $Ba_{0.4}Sr_{0.6}TiO_3$-MgO composite prepared by spark plasma sintering. J Eur Ceram Soc 35. https://doi.org/10.1016/j.jeurceramsoc.2014.11.022
34. Touzin M, Gœuriot D, Fitting HJ, Guerret-Piecourt C, Juvé D, Tréheux D (2007) Relationships between dielectric breakdown resistance and charge transport in alumina materials—Effects of the microstructure. J Eur Ceram Soc 27:1193. https://doi.org/10.1016/j.jeurceramsoc.2006.05.047
35. Rousselle M, Ansart F, Hérisson de Beauvoir T, Fradet G, Estournès C (2021) Phase evolution and sinterability of lanthanum phosphate – towards a below 600 °C spark plasma sintering. J Eur Ceram Soc 41: 7261. https://doi.org/10.1016/j.jeurceramsoc.2021.07.014
36. Hsiang H-I, Hsi C-S, Huang C-C, Fu S-L (2008) Sintering behavior and dielectric properties of $BaTiO_3$ ceramics with glass addition for internal capacitor of LTCC. J Alloy Compd 459:307. https://doi.org/10.1016/j.jallcom.2007.04.218
37. Xu Q, Zhan D, Huang D-P, Liu H-X, Chen W, Zhang F (2013) Effect of MgO-CaO-Al_2O_3-SiO_2 glass additive on dielectric properties of $Ba_{0.95}Sr_{0.05}Zr_{0.2}Ti_{0.8}O_3$ ceramics. J Alloy Compd 558:77. https://doi.org/10.1016/j.jallcom.2012.12.164
38. Young A, Hilmas G, Zhang S, Schwartz R (2007) Effect of liquid-phase sintering on the breakdown strength of barium titanate. J Am Ceram Soc 90:1504. https://doi.org/10.1111/j.1551-2916.2007.01637.x
39. Zhang Q, Wang L, Luo J, Tang Q, Du J (2009) Improved energy storage density in barium strontium titanate by addition of BaO-SiO_2-B_2O_3 glass. J Am Ceram Soc 92:1871. https://doi.org/10.1111/j.1551-2916.2009.03109.x
40. Lee W-H, Su CY (2007) Improvement in the temperature stability of a $BaTiO_3$-based multilayer ceramic capacitor by constrained sintering. J Am Ceram Soc 90: 3345. https://doi.org/10.1111/j.1551-2916.2007.01900.x
41. Kim C-H, Park K-J, Yoon Y-J, Hong M-H, Hong J-O, Hur K-H (2008) Role of yttrium and magnesium in the formation of core-shell structure of $BaTiO_3$ grains in MLCC. J Eur Ceram Soc 28:1213. https://doi.org/10.1016/j.jeurceramsoc.2007.09.042
42. Liu Y, Cui B, Wang Y, Ma R, Shangguan M, Zhao X, Wang S, Li Q, Wang Y (2016) Core-shell structure and dielectric properties

of $Ba_{0.991}Bi_{0.006}TiO_3$@$Nb_2O_5$-$Co_3O_4$ ceramics. J Am Ceram Soc 99: 1664. https://doi.org/10.1111/jace.14154

43. Liu B, Wang X, Zhao Q, Li L (2015) Improved energy storage properties of fine-crystalline $BaTiO_3$ ceramics by coating powders with Al_2O_3 and SiO_2. J Am Ceram Soc 98. https://doi.org/10.1111/jace.13614
44. Ma R, Cui B, Wang Y, Wang S, Wang Y (2019) The energy storage properties of fine-grained $Ba_{0.8}Sr_{0.2}Zr_{0.1}Ti_{0.9}O_3$ ceramics enhanced by MgO and ZnO-B_2O_3-SiO_2 coatings. Mater Res Bull 111:311. https://doi.org/10.1016/j.materresbull.2018.11.033
45. Wang J, Jiang S, Jiang D, Tian J, Li Y, Wang Y (2012) Microstructural design of $BaTiO_3$-based ceramics for temperature-stable multilayer ceramic capacitors. Ceram Int 38:5853. https://doi.org/10.1016/j.ceramint.2012.04.036
46. Shangguan M, Cui B, Ma R, Wang Y (2016) Production of $Ba_{0.991}Bi_{0.006}TiO_3$@ZnO-$B_2O_3$-$SiO_2$ ceramics with a high dielectric constant, a core–shell structure, and a fine-grained microstructure by means of a sol-precipitation method. Ceram Int 42. https://doi.org/10.1016/j.ceramint.2016.01.143
47. Mornet S, Elissalde C, Hornebecq V, Bidault O, Duguet E, Brisson A, Maglione M (2005) Controlled growth of silica shell on $Ba_{0.6}Sr_{0.4}TiO_3$ nanoparticles used as precursors of ferroelectric composites. Chem Mater 17:4530. https://doi.org/10.1021/cm050884r
48. Moshtaghioun B, Peña J (2019) Non-Hall-Petch hardness dependence in ultrafine fibrous $MgAl_2O_4$-MgO eutectic ceramics fabricated by the laser-heated floating zone (LFZ) method. J Eur Ceram Soc 39:3208. https://doi.org/10.1016/j.jeurceramsoc.2019.04.015
49. Shannon RD (1967) Synthesis of some new perovskites containing indium and thallium. Inorg Chem 6:1474. https://doi.org/10.1021/ic50054a009
50. Tombácz E, Majzik A, Horvát Z, Illés E (2004) The role of reactive surface sites and complexation by humic acids in the interaction of clay mineral and iron oxide particles. Organic Geochemistry 35:257. https://doi.org/10.1016/j.orggeochem.2003.11.002
51. Fisher JG, Lee BK, Choi SY, Wang SM, Kang SJL (2006) Inhibition of abnormal grain growth in $BaTiO_3$ by addition of Al_2O_3. J Eur Ceram Soc 26:1619. https://doi.org/10.1016/j.jeurceramsoc.2005.03.234
52. Tura V, Mitoseriu L (1994) Polarization reversal in (Nb, Co)-doped $BaTiO_3$ ceramics. Phys Lett A 189:327. https://doi.org/10.1016/0375-9601(94)90104-X
53. Zhang J, Ji L, Jia X, Wang J, Zhai J, Zhou Y (2015) Crystal structure and effective dielectric response of $Ba_{0.5}Sr_{0.5}TiO_3$-MgO composites synthesized in situ process. J Am Ceram Soc 98:97. https://doi.org/10.1111/jace.13242
54. Cheng B, Su B, Holmes J, Button T, Gabbay M, Fantozzi G (2002) Dielectric and mechanical losses in $(Ba,Sr)TiO_3$ systems. J Electroceram 9:17. https://doi.org/10.1023/A:1021633917071
55. Fisher JG, Lee BK, Brancquart A, Choi SY, Kang SJ (2005) Effect of Al_2O_3 dopant on abnormal grain growth in $BaTiO_3$. J Eur Ceram Soc 25:2033. https://doi.org/10.1016/j.jeurceramsoc.2005.03.065
56. Wu L, Wang X, Li L (2016) Core-shell $BaTiO_3$@$BiScO_3$ particles for local graded dielectric ceramics with enhanced temperature stability and energy storage capability. J Alloys Compd 688:113. https://doi.org/10.1016/j.jallcom.2016.07.057
57. Cao SY, Zhu JT, Chen Q, Liu JT, Wu CY, Li LL, Xu J, Yan HX, Gao F (2022) Exploration about superior anti-counterfeiting ability of Sm^{3+} doped $KSr_2Nb_5O_{15}$ photochromic ceramics: Origin and atomic-scale mechanism. J Materiomics 8:38–46. https://doi.org/10.1016/j.jmat.2021.06.001
58. Zhang L, Zhong WL, Wang CL, Peng YP, Wang YG (1999) Size dependence of dielectric properties and structural metastability in ferroelectrics. Eur Phys J B 11:565. https://doi.org/10.1007/s100510051184